A&A 558, A58 (2013)
DOI: 10.1051/0004-6361/201321944

Astronomy & Astrophysics

Deep observations of O_2 toward a low-mass protostar with *Herschel*-HIFI⋆,⋆⋆,⋆⋆⋆

Umut A. Yıldız[1], Kinsuk Acharyya[2], Paul F. Goldsmith[3], Ewine F. van Dishoeck[1,4], Gary Melnick[5], Ronald Snell[6], René Liseau[7], Jo-Hsin Chen[3], Laurent Pagani[8], Edwin Bergin[9], Paola Caselli[10,11], Eric Herbst[12], Lars E. Kristensen[5], Ruud Visser[9], Dariusz C. Lis[13], and Maryvonne Gerin[14]

[1] Leiden Observatory, Leiden University, PO Box 9513, 2300 RA Leiden, The Netherlands
e-mail: yildiz@strw.leidenuniv.nl
[2] S.N. Bose National Centre for Basic Sciences, 700098 Kolkata, Salt Lake, India
[3] Jet Propulsion Laboratory, California Institute of Technology, 4800 Oak Grove Drive, Pasadena, CA 91109, USA
[4] Max Planck Institut für Extraterrestrische Physik, Giessenbachstrasse 1, 85748 Garching, Germany
[5] Harvard-Smithsonian Center for Astrophysics, 60 Garden Street, Cambridge, MA 02138, USA
[6] Department of Astronomy, LGRT 619, University of Massachusetts, 710 North Pleasant Street, Amherst, MA 01003, USA
[7] Dept. of Earth & Space Sciences, Chalmers University of Technology, Onsala Space Observatory, 43992 Onsala, Sweden
[8] LERMA & UMR 8112 du CNRS, Observatoire de Paris, 61 Av. de l'Observatoire, 75014 Paris, France
[9] Department of Astronomy, University of Michigan, 500 Church Street, Ann Arbor, MI 48109-1042, USA
[10] School of Physics and Astronomy, University of Leeds, Leeds LS2 9JT, UK
[11] INAF-Osservatorio Astrofisico di Arcetri, Largo E. Fermi 5, 50125 Firenze, Italy
[12] Departments of Chemistry, Astronomy, and Physics, The University of Virginia, Charlottesville, Virginia, USA
[13] California Institute of Technology, Cahill Center for Astronomy and Astrophysics 301-17, Pasadena, CA 91125, USA
[14] LRA/LERMA, CNRS, UMR 8112, Observatoire de Paris & École Normale Supérieure, 24 rue Lhomond, 75231 Paris Cedex 5, France

Received 22 May 2013 / Accepted 26 July 2013

ABSTRACT

Context. According to traditional gas-phase chemical models, O_2 should be abundant in molecular clouds, but until recently, attempts to detect interstellar O_2 line emission with ground- and space-based observatories have failed.
Aims. Following the multi-line detections of O_2 with low abundances in the Orion and ρ Oph A molecular clouds with *Herschel*, it is important to investigate other environments, and we here quantify the O_2 abundance near a solar-mass protostar.
Methods. Observations of molecular oxygen, O_2, at 487 GHz toward a deeply embedded low-mass Class 0 protostar, NGC 1333-IRAS 4A, are presented, using the Heterodyne Instrument for the Far Infrared (HIFI) on the *Herschel* Space Observatory. Complementary data of the chemically related NO and CO molecules are obtained as well. The high spectral resolution data are analysed using radiative transfer models to infer column densities and abundances, and are tested directly against full gas-grain chemical models.
Results. The deep HIFI spectrum fails to show O_2 at the velocity of the dense protostellar envelope, implying one of the lowest abundance upper limits of O_2/H_2 at $\leq 6 \times 10^{-9}$ (3σ). The O_2/CO abundance ratio is less than 0.005. However, a tentative (4.5σ) detection of O_2 is seen at the velocity of the surrounding NGC 1333 molecular cloud, shifted by 1 km s^{-1} relative to the protostar. For the protostellar envelope, pure gas-phase models and gas-grain chemical models require a long pre-collapse phase (~0.7–1 $\times 10^6$ years), during which atomic and molecular oxygen are frozen out onto dust grains and fully converted to H_2O, to avoid overproduction of O_2 in the dense envelope. The same model also reproduces the limits on the chemically related NO molecule if hydrogenation of NO on the grains to more complex molecules such as NH_2OH, found in recent laboratory experiments, is included. The tentative detection of O_2 in the surrounding cloud is consistent with a low-density PDR model with small changes in reaction rates.
Conclusions. The low O_2 abundance in the collapsing envelope around a low-mass protostar suggests that the gas and ice entering protoplanetary disks is very poor in O_2.

Key words. astrochemistry – stars: formation – ISM: molecules – ISM: individual objects: NGC 1333 IRAS 4A

1. Introduction

Even though molecular oxygen (O_2) has a simple chemical structure, it remains difficult to detect in the interstellar medium after many years of searches (Goldsmith et al. 2011, and references therein). Oxygen is the third most abundant element in the Universe, after hydrogen and helium, which makes it very important in terms of understanding the formation and evolution of the chemistry in astronomical sources.

⋆ *Herschel* is an ESA space observatory with science instruments provided by European-led Principal Investigator consortia and with important participation from NASA.
⋆⋆ Appendices are available in electronic form at http://www.aanda.org
⋆⋆⋆ Reduced spectra (FITS files) are only available at the CDS via anonymous ftp to cdsarc.u-strasbg.fr (130.79.128.5) or via http://cdsarc.u-strasbg.fr/viz-bin/qcat?J/A+A/558/A58

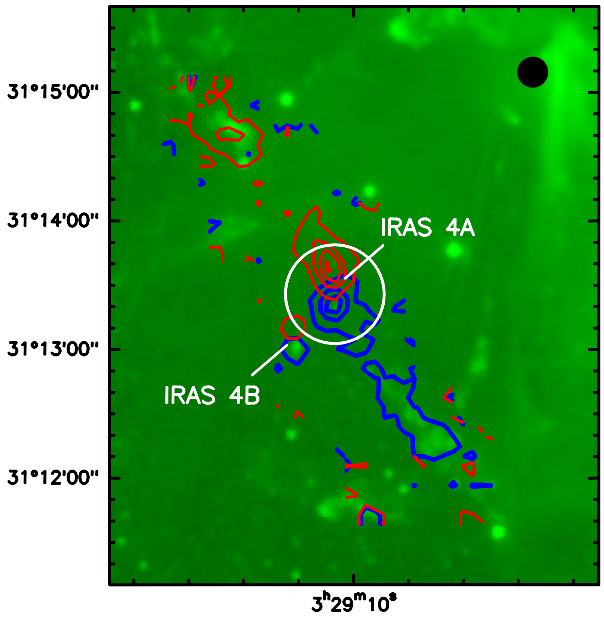

Fig. 1. *Spitzer*/IRAC1 (Gutermuth et al. 2008) and CO 6–5 contours (Yıldız et al. 2012) are overlaid to illustrate the NGC 1333 IRAS 4A and 4B protostars. The white circle in the center represents the observed HIFI beam of 44″ centred on IRAS 4A, illustrating that it partially overlaps with the outer part of the IRAS 4B envelope. The contours indicate the outflows, with levels starting from 15 K km s^{-1} with an increasing step size of 30 K km s^{-1}. Blue and red velocity ranges are selected from –20 to 2.7 and from 10.5 to 30 km s^{-1}, respectively. The black dot on upper right corner shows the beam size of the CO 6–5 data.

Pure gas-phase chemistry models suggest a steady-state abundance of $X(O_2) \approx 7 \times 10^{-5}$ relative to H_2 (e.g., Table 9 of Woodall et al. 2007), however observations show that the abundance is several orders of magnitude lower than these model predictions. Early (unsuccessful) ground-based searches of O_2 were done through the $^{16}O^{18}O$ isotopologue (Goldsmith et al. 1985; Pagani et al. 1993), for which some of the lines fall in a transparent part of the atmosphere. Due to the oxygen content of the Earth's atmosphere, it is however best to observe O_2 from space. Two previous space missions, the Submillimeter Wave Astronomy Satellite (SWAS; Melnick et al. 2000) and the *Odin* Satellite (Nordh et al. 2003) were aimed at detecting and studying interstellar molecular oxygen through specific transitions. SWAS failed to obtain a definitive detection of O_2 at 487 GHz toward nearby clouds (Goldsmith et al. 2000), whereas *Odin* observations of O_2 at 119 GHz gave upper limits of $\leq 10^{-7}$ (Pagani et al. 2003), except for the ρ Ophiuchi A cloud ($X(O_2) \sim 5 \times 10^{-8}$; Larsson et al. 2007).

The *Herschel* Space Observatory provides much higher spatial resolution and sensitivity than previous missions and therefore allows very deep searches for O_2. Recently, *Herschel*-HIFI provided firm multi-line detections of O_2 in the Orion and ρ Oph A molecular clouds (Goldsmith et al. 2011; Liseau et al. 2012). The abundance was found to range from $X(O_2) \simeq 10^{-6}$ (in Orion) to $X(O_2) \simeq 5 \times 10^{-8}$ (in ρ Oph A). The interpretation of the low abundance is that oxygen atoms are frozen out onto grains and transformed into water ice that coats interstellar dust, leaving little atomic O in the gas to produce O_2 (Bergin et al. 2000). So far, O_2 has only been found in clouds where (external) starlight has heated the dust and prevented atomic O from sticking onto the grains and being processed into H_2O as predicted by theory (Hollenbach et al. 2009) or where O_2 is enhanced in postshock gas (Goldsmith et al. 2011). Not every warm cloud has O_2, however. Melnick et al. (2012) report a low upper limit on gaseous O_2 toward the dense Orion Bar photon-dominated region (PDR).

Although the detection of O_2 in some molecular clouds is significant, these data tell little about the presence of O_2 in regions where solar systems may form. It is therefore important to also make deep searches for O_2 near solar-mass protostars to understand the origin of molecular oxygen in protoplanetary disks and eventually (exo-)planetary atmospheres. Even though the bulk of the O_2 in the Earth's atmosphere arises from microorganisms, the amount of O_2 that could be delivered by cometesimal impacts needs to be quantified. In the present paper, a nearby low-mass deeply embedded protostar, NGC 1333 IRAS 4A, is targeted, which has one of the highest line of sight hydrogen column densities of $N(H_2) \sim 10^{24}$ cm^{-2} derived from dust modeling (Jørgensen et al. 2002; Kristensen et al. 2012). Since the *Herschel* beam size at 487 GHz is a factor of ~6 smaller than that of SWAS, *Herschel* is much more sensitive to emission from these compact sources. Protostars also differ from dense clouds or PDRs by the fact that a significant fraction of the dust is heated internally by the protostellar luminosity to temperatures above those needed to sublimate O and O_2.

NGC 1333 IRAS 4A is located in the southeast part of the NGC 1333 region, together with IRAS 4B (henceforth IRAS 4A and IRAS 4B). A distance of 235 ± 18 pc is adopted based on VLBI parallax measurements of water masers in the nearby source SVS 13 (Hirota et al. 2008). Both objects are classified as deeply-embedded Class 0 low-mass protostars (André & Montmerle 1994) and are well-studied in different molecular lines such as CO, SiO, H_2O and CH_3OH (e.g., Blake et al. 1995; Lefloch et al. 1998; Bottinelli et al. 2007; Yıldız et al. 2012; Kristensen et al. 2010). Figure 1 shows a CO J = 6–5 contour map obtained with APEX (Yıldız et al. 2012) overlaid on a *Spitzer*/IRAC1 (3.6 μm) image (Gutermuth et al. 2008). Both IRAS 4A and IRAS 4B have high-velocity outflows seen at different inclinations. The projected separation between the centers of IRAS 4A and IRAS 4B is 31″ (~7300 AU). The source IRAS4A was chosen for the deep O_2 search because of its chemical richness and high total column density. In contrast to many high-mass protostars, it has the advantage that even very sensitive spectra do not show line confusion.

On a larger scale, early millimeter observations of CO and ^{13}CO J = 1–0 by Loren (1976) and Liseau et al. (1988) found two (possibly colliding) clouds in the NGC 1333 region, with velocities separated by up to 2 km s^{-1}. Černis (1990) used extinction mapping in the NGC 1333 region to confirm the existence of two different clouds. The IRAS 4A protostellar envelope is centred at the lower velocity around V_{LSR} = 7.0 km s^{-1}, whereas the lower (column) density cloud appears around V_{LSR} = 8.0 km s^{-1}. The high spectral resolution of our data allows O_2 to be probed in both clouds. Optically thin isotopologue data of $C^{18}O$ J = 1–0 up to J = 5–4 are used to characterize the conditions in the two components. Note that these velocities do not overlap with those of the red outflow lobe, which start at V_{LSR} = +10.5 km s^{-1}.

We present here the first sensitive observations of the O_2 3_3–1_2 487 GHz line towards a deeply embedded low-mass Class 0 protostar, observed with *Herschel*-HIFI. Under a wide range of conditions, the O_2 line at 487 GHz is the strongest, therefore this line is selected for long integration. The data are complemented by ground-based observations of CO isotopologues and NO using the IRAM 30 m and JCMT telescopes. The CO data are used to characterize the kinematics and physical conditions in the clouds as well as the column of gas where CO is not frozen out. Since the O_2 ice has a very similar binding

Table 1. Overview of the observed lines.

Molecule	Transition	E_u/k_B [K]	A_{ul} [s^{-1}]	Frequency [GHz]
O_2	$N_J = 3_3$–1_2	26.4	8.657×10^{-9}	487.2492640
$C^{18}O$	J = 1–0	5.3	6.266×10^{-8}	109.7821734
$C^{18}O$	J = 3–2	31.6	2.172×10^{-6}	329.3305525
$C^{18}O$	J = 5–4	79.0	1.062×10^{-5}	548.8310055
NO (1)	J = 5/2–3/2, F = 3/2–1/2	19.3	1.387×10^{-6}	250.8169540
NO (2)	J = 5/2–3/2, F = 5/2–3/2	19.3	1.553×10^{-6}	250.8155940
NO (3)	J = 5/2–3/2, F = 7/2–5/2	19.3	1.849×10^{-6}	250.7964360
NO (4)	J = 5/2–3/2, F = 3/2–3/2	19.3	4.437×10^{-7}	250.7531400

energy as the CO ice, either in pure or mixed form (Collings et al. 2004; Acharyya et al. 2007), CO provides a good reference for O_2. NO is chosen because it is a related species that could help to constrain the chemistry of O_2. In the gas, O_2 can be produced from atomic O through the reaction (Herbst & Klemperer 1973; Black & Smith 1984)

$$O + OH \rightarrow O_2 + H \quad (1)$$

with rate constants measured by Carty et al. (2006). The nitrogen equivalent of Eq. (1) produces NO through

$$N + OH \rightarrow NO + H. \quad (2)$$

The outline of the paper is as follows. Section 2 describes the observations and the telescopes where the data were obtained. Results from the observations are presented in Sect. 3. The deep HIFI spectrum reveals a non-detection of O_2 at the velocity of the central protostellar source. However, a tentative (4.5σ) detection is found originating from the surrounding NGC 1333 cloud at $V_{LSR} = 8$ km s^{-1}. In Sect. 3, a physical model of the source coupled with line radiative transfer is used to infer the gas-phase abundance profiles of CO, O_2 and NO in the protostellar envelope that are consistent with the data ("backward" or retrieval modeling, see Doty et al. 2004 for terminology). Forward modeling using a full gas-grain chemical code coupled with the same physical model is subsequently conducted to interpret the non-detection in Sect. 4. In Sect. 5, the implications for the possible detection in the 8 km s^{-1} component are discussed and in Sect. 6, the conclusions from this work are summarized.

2. Observations

The molecular lines observed towards the IRAS 4A protostar ($3^h29^m10\overset{s}{.}5$, +31°13′30.″9 (J2000); Jørgensen et al. 2009) are presented in Table 1 with the corresponding frequencies, upper level energies (E_u/k_B), and Einstein A coefficients. The O_2 data were obtained with the Heterodyne Instrument for the Far-Infrared (HIFI; de Graauw et al. 2010) onboard the *Herschel* Space Observatory (Pilbratt et al. 2010), in the context of the "*Herschel* Oxygen Project" (HOP) open-time key program, which aims to search for O_2 in a range of star-forming regions and dense clouds (Goldsmith et al. 2011). Single pointing observations at the source position were carried out on operation day OD 445 on August 1 and 2, 2010 with *Herschel* obsids of 1342202025–. . .–1342202032. The data were taken in dual-beam switch (DBS) mode using the HIFI band 1a mixer with a chop reference position located 3′ from the source position. Eight observations were conducted with an integration time of 3477 s each, and eight different local-oscillator (LO) tunings were used in order to allow deconvolution of the signal from the image side band. The LO tunings are shifted by 118 MHz up to 249 MHz. Inspection of the data shows no contamination from the reference position in any of the observations, nor from the image side-band. The total integration time is thus 7.7 h (27 816 s) for the on+off source integration.

The central frequency of the O_2 3_3–1_2 line is 487.249264 GHz with an upper level energy of $E_u = 26.4$ K and an Einstein A coefficient of 8.657×10^{-9} s^{-1} (Drouin et al. 2010). In HIFI, two spectrometers are in operation, the "Wide Band Spectrometer" (WBS) and the "High Resolution Specrometer" (HRS) with resolutions of 0.31 km s^{-1} and 0.073 km s^{-1} at 487 GHz, respectively. Owing to the higher noise ranging from a factor of 1.7 up to 4.7 of the HRS compared with the WBS, only WBS observations were used in the analysis. There is a slight difference between the pointings of the H and V polarizations in HIFI, but this difference of ΔHV (–6.″2, +2.″2; Roelfsema et al. 2012) for Band 1 is small enough to be neglected relative to the beam size of 44″ (FWHM). Spectra from both polarizations were carefully checked for differences in intensities of other detected lines but none were found. Therefore the two polarizations were averaged to improve the signal to noise ratio.

Data processing started from the standard HIFI pipeline in the *Herschel* Interactive Processing Environment (HIPE[1]) ver. 8.2.1 (Ott 2010), where the V_{LSR} precision is of the order of a few m s^{-1}. The lines suffer from significant standing waves in each of the observations. Therefore a special task `FitHifiFringe` in HIPE was used to remove standing waves. The fitting routine was applied to each observation one by one and it successfully removed a large part of the standing waves. Further processing and analysis was done using the GILDAS-`CLASS`[2] software. A first order polynomial was applied to all observations, which were subsequently averaged together. The standard antenna temperature scale T_A^* is corrected to the main beam temperature T_{MB} (Kutner & Ulich 1981) by applying the efficiency of 0.76 for HIFI band 1a (Roelfsema et al. 2012, Fig. 2).

To understand and constrain the excitation and chemistry of O_2, complementary transitions in NO and $C^{18}O$ were observed. Nitrogen monoxide (NO) was observed with the *James Clerk Maxwell* Telescope (JCMT[3]) by using Receiver A with a beam size of 20″ as part of the M10BN05 observing program. The total integration time for this observation was 91 min. $C^{18}O$ J = 1–0 was observed with the IRAM 30 m telescope[4] using a frequency-switch mode over an area of 1′ × 1′ in a 22″ beam. A $C^{18}O$ J = 3–2 spectrum was extracted from the large NGC 1333 map of Curtis et al. (2010), which was observed with the HARPB instrument at JCMT with position switch-mode (off position coordinate: $3^h29^m00\overset{s}{.}0$, +31°52′30.″0; J2000) in a 15″ beam (also in Yıldız et al. 2012). Both maps were convolved to a beam of 44″ in order to directly compare with the O_2 spectra in the same beam. The 15″ beam spectra presented in Yıldız et al. (2012) show primarily the 7.0 km s^{-1} component. The $C^{18}O$ J = 5–4 line was observed with *Herschel*-HIFI within

[1] HIPE is a joint development by the Herschel Science Ground Segment Consortium, consisting of ESA, the NASA Herschel Science Center, and the HIFI, PACS and SPIRE consortia.

[2] http://www.iram.fr/IRAMFR/GILDAS/

[3] The JCMT is operated by the Joint Astronomy Centre on behalf of the Science and Technology Facilities Council of the United Kingdom, the Netherlands Organisation for Scientific Research, and the National Research Council of Canada.

[4] Based on observations carried out with the IRAM 30 m Telescope. IRAM is supported by INSU/CNRS (France), MPG (Germany) and IGN (Spain).

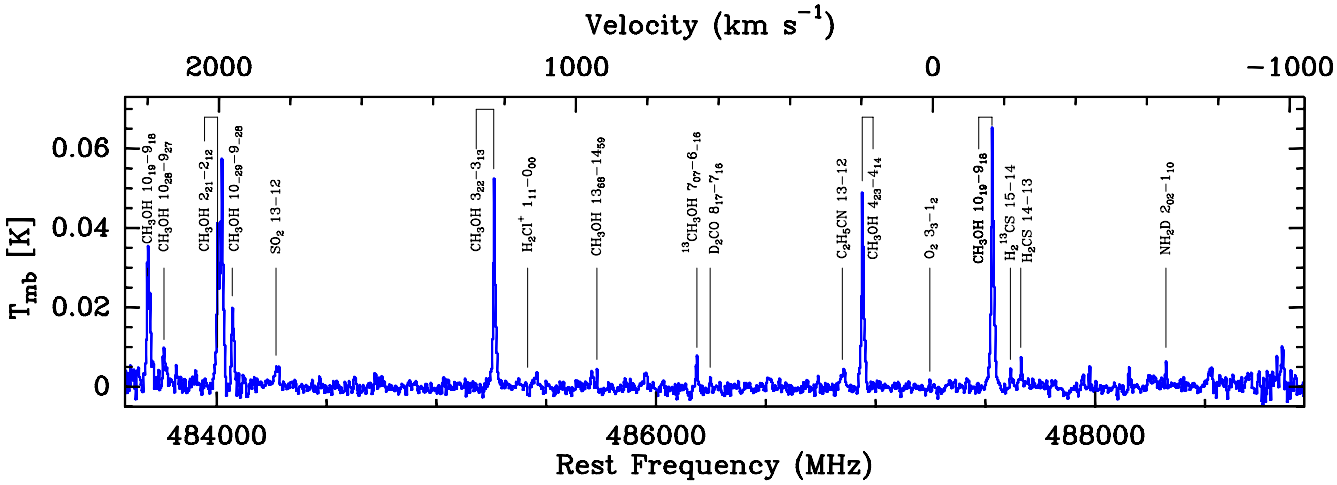

Fig. 2. Full spectrum taken with HIFI, with the *H*- and *V*-polarization spectra averaged. The frequency range is 483.59 GHz to 488.94 GHz from left to right. The entire bandwidth is 5.35 GHz. The O_2 line is centred near $V_{LSR} = 7.0$ km s^{-1}. A blow-up of the spectrum is presented in Fig. A.1.

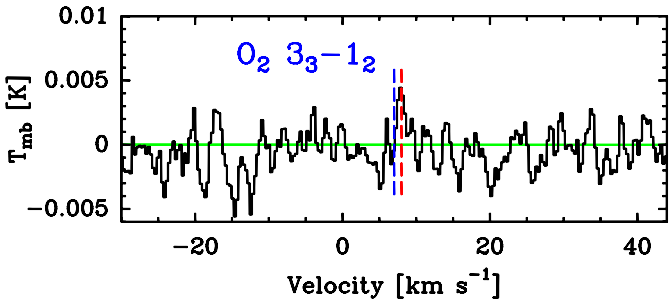

Fig. 3. Spectrum of Fig. 2 magnified around the O_2 3_3–1_2 line. The blue dashed line indicates the LSR velocity of the IRAS 4A envelope at 7.0 km s^{-1}and the red dashed line shows the velocity at 8.0 km s^{-1}.

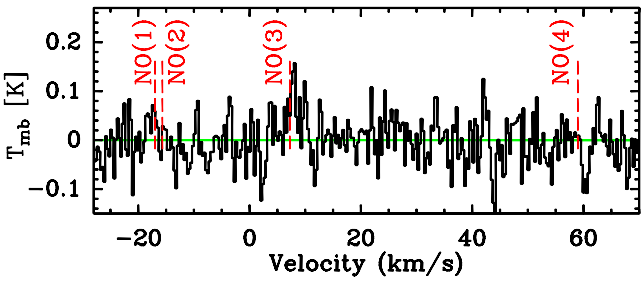

Fig. 4. Spectrum of the NO J = 5/2–3/2 transitions showing the location of four hyperfine (HF) components, where the details of the lines are given in Table 1. The spectrum is centred on the NO (3) (HF) component.

the "Water in Star-forming regions with *Herschel*" (WISH) guaranteed-time key program (van Dishoeck et al. 2011) in a beam size of 40″ and reported in Yıldız et al. (2012). Beam efficiencies are 0.77, 0.63, and 0.76 for the 1–0, 3–2, and 5–4 lines, respectively. The calibration uncertainty for HIFI band 1a is 15%, whereas it is 20% for the IRAM 30 m and JCMT lines.

The HIFI beam size at 487 GHz of ∼44″ corresponds to a 5170 AU radius for IRAS 4A at 235 pc (Fig. 1, white circle). It therefore overlaps slightly with the dense envelope around IRAS 4B (see also Fig. 13 in Yıldız et al. 2012) but this is neglected in the analysis. The NO data were taken as a single pointing observation, therefore the beam size is ∼20″, about half of the diameter covered with the O_2 observation.

3. Results

In Fig. 2, the full *Herschel*-HIFI WBS spectrum is presented. Although the bandwidth of the WBS data is 4 GHz, the entire spectrum covers 5.35 GHz as a result of combining eight different observations where the LO frequencies were slightly shifted in each of the settings. The rms of this spectrum is 1.3 mK in 0.35 km s^{-1} bin, therefore many faint lines are detected near the main targeted O_2 3_3–1_2 line. These lines include some methanol (CH_3OH) lines, together with e.g., SO_2, NH_2D, and D_2CO lines. These lines are shown in Fig. A.1 in detail, and are tabulated with the observed information in Table A.1.

3.1. O_2

A blow-up of the HIFI spectrum centred around the O_2 $N_J = 3_3$–1_2 at 487 GHz position is presented in Fig. 3. The source velocity of IRAS 4A is $V_{LSR} = 7.0$ km s^{-1} as determined from many $C^{18}O$ lines (Yıldız et al. 2012), and is indicated by the blue dashed line in the figure. This spectrum of 7.7 h integration time staring at the IRAS 4A source position is still not sufficient for a firm detection of the O_2 line at 487 GHz at the source velocity. However, a tentative detection at $V_{LSR} = 8.0$ km s^{-1} (red dashed line in Fig. 3) is seen and will be discussed in more detail in Sect. 5.

3.2. NO

In Fig. 4, the JCMT spectrum covering the hyperfine components of the NO J = 5/2–3/2 transitions are presented. For this specific transition, the expected ratios of the line intensities in the optically thin limit are NO (1):NO (2):NO (3):NO (4) = 75:126:200:24. The JCMT observations have an rms of 46 mK in 0.3 km s^{-1} bin and 4σ emission is detected only at the intrinsically strongest hyperfine transition, NO (3), with an integrated intensity of 0.18 K km s^{-1} centred at $V_{LSR} = 8.0$ km s^{-1}. No emission is detected for the $V_{LSR} = 7.0$ km s^{-1} component, however 3σ upper limit values are provided in Table 2.

Table 2. Summary of the observed line intensities in a 44″ beam.

Molecule	Transition	Telescope/ Instrument	$\int T_{MB} dV$ [K km s^{-1}]	T_{peak} [K]	*FWHM* [km s^{-1}]	$\int T_{MB} dV$ [K km s^{-1}]	T_{peak} [K]	*FWHM* [km s^{-1}]	Rms [mK]
			7.0 km s^{-1} component[a]			8.0 km s^{-1} component[b]			
O_2	$N_J = 3_3$–1_2	*Herschel*-HIFI	<0.0027[c]	…	…	0.0069	0.0046	1.3	1.3[d]
$C^{18}O$	J = 1–0	IRAM 30 m-EMIR	1.30	1.38	0.9	2.25	2.35	0.9	26[e]
$C^{18}O$	J = 3–2	JCMT-HARP-B	1.32	1.36	0.9	1.67	1.74	0.9	99[e]
$C^{18}O$	J = 5–4	*Herschel*-HIFI	0.39	0.36	1.0	0.13	0.13	1.0	10[e]
NO (3)	J = 5/2–3/2, F = 7/2–5/2	JCMT-RxA	<0.15[c]	…	…	0.18	0.16	2.9	46[e]

Notes. The values are calculated through a fit to the lines. [(a)] V_{LSR} = 7.0 km s^{-1} component. [(b)] V_{LSR} = 8.0 km s^{-1} component. [(c)] 3σ upper limit. [(d)] In 0.35 km s^{-1} bins. [(e)] In 0.3 km s^{-1} bins.

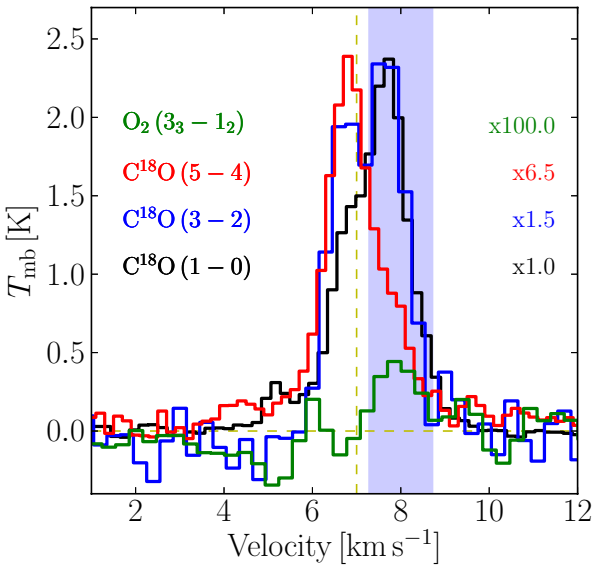

Fig. 5. O_2 3_3–1_2 spectrum overplotted with the $C^{18}O$ 1–0, 3–2, and 5–4 lines in a 44″ beam. The $C^{18}O$ spectra are scaled to the same peak intensity. Note the shift in velocity from 8.0 to 7.0 km s^{-1} with increasing J.

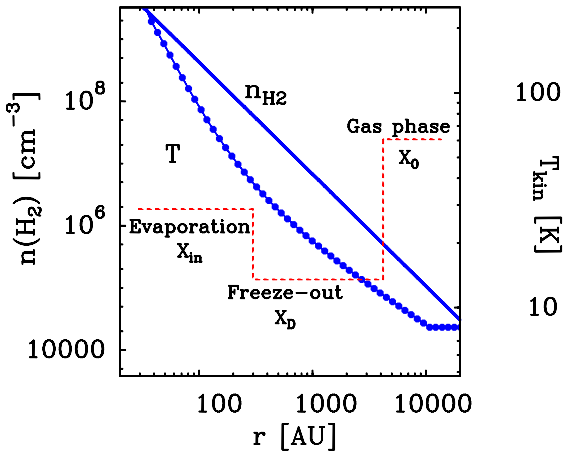

Fig. 6. Variation of number density, which follows a power-law density profile and temperature of the NGC 1333 IRAS 4A envelope as function of radial distance, taken from the model of Kristensen et al. (2012). Overplotted red dashed line shows the limits of drop abundance profile by radius obtained by the $C^{18}O$ modeling as explained in Sect. 3.4.2.

3.3. $C^{18}O$

Figure 5 shows the $C^{18}O$ 1–0, 3–2, and 5–4 lines overplotted on the O_2 line. The peak of the $C^{18}O$ emission shifts from V_{LSR} = 8.0 km s^{-1} to 7.0 km s^{-1} as J increases. The $C^{18}O$ 1–0 line is expected to come primarily from the surrounding cloud at 8.0 km s^{-1} due to the low energy of the transition (E_{up} = 5.3 K). On the other hand, the 5–4 line has higher energy (E_{up} = 79 K), therefore traces the warmer parts of the protostellar envelope at 7.0 km s^{-1}. As a sanity check, the ^{13}CO 1–0, 3–2, and 6–5 transitions from Yıldız et al. (2012) were also inspected and their profiles are consistent with those of the $C^{18}O$ lines, however they are not included here due to their high opacities. The integrated intensities $\int T_{mb} dV$ for each of the 7.0 km s^{-1} and 8.0 km s^{-1} components are given in Table 2.

3.4. Column densities and abundances

3.4.1. Constant excitation temperature results

A first simple estimate of the O_2 abundance limit in the IRAS 4A protostellar envelope (V_{LSR} = 7.0 km s^{-1} component) is obtained by computing column densities within the 44″ beam. The collisional rate coefficients for the O_2 3_3–1_2 line give a critical density of $n_{cr} = 1 \times 10^3$ cm^{-3} for low temperatures (Lique 2010; Goldsmith et al. 2011). The density at the 5000 AU radius corresponding to this beam is found to be 4×10^5 cm^{-3} based on the spherical power-law density model of Kristensen et al. (2012, see also Fig. 6 and below). This value is well above the critical density, implying that the O_2 excitation is thermalized. High densities are independently confirmed by the detection of many high excitation lines from molecules with large dipole moments in this source (e.g., Jørgensen et al. 2005; Maret et al. 2005). The width of the O_2 3_3–1_2 line is taken to be similar to that of $C^{18}O$, $\Delta V \approx 1.0$ km s^{-1}. The O_2 line is assumed to be optically thin and a temperature of 30 K is used. The 3σ O_2 column density limit at V_{LSR} = 7.0 km s^{-1} is then $N(O_2) = 1.1 \times 10^{15}$ cm^{-2} assuming Eqs. (2) and (3) from Yıldız et al. (2012).

The total H_2 column density of the 7.0 km s^{-1} component in the 44″ beam is computed from the model of Kristensen et al. (2012) through $N_{X,beam} = \int\int n_X(z,b) dz G(b) 2\pi b db / \int G(b) 2\pi b db$, where b is the impact parameter, and $G(b)$ is the beam response function. The resulting value is $N(H_2) = 2.1 \times 10^{23}$ cm^{-2}, which is an order of magnitude lower than the pencil-beam H_2 column density of 1.9×10^{24} cm^{-2}. Using the 44″-averaged H_2 column density implies an abundance limit $X(O_2) \leq 5.7 \times 10^{-9}$. This observation therefore provides the lowest limit on the O_2 abundance

Table 3. Summary of column densities in a 44″ beam.

Molecule	Column density [cm^{-2}]		Abundance w.r.t. H_2	
	N(7 km s^{-1})	N(8 km s^{-1})	X(7 km s^{-1})	X(8 km s^{-1})
O_2	$<1.2\times10^{15}$ [a]	$(2.8–4.3)\times10^{15}$	$\leq5.7\times10^{-9}$	$(1.3–2.1)\times10^{-8}$
$C^{18}O$	$(3.2–6.1)\times10^{14}$	$(1.8–2.3)\times10^{15}$	$(1.7–3.0)\times10^{-9}$	$(4.3–2.2)\times10^{-7}$
NO	$<1.9\times10^{14}$ [a]	2.3×10^{14}	$\leq9.0\times10^{-10}$	2.3×10^{-8}
H_2	2.1×10^{23} [b]	1×10^{22} [c]	...	...

Notes. See text for the conditions used for the calculations. [a] 3σ column density limit. [b] Beam averaged H_2 column density in a 44″ beam obtained from the model of Kristensen et al. (2012). [c] Computed using the average $C^{18}O$ column density and abundance ratios of CO/H_2 = 10^{-4} and CO/$C^{18}O$ = 550 (Wilson & Rood 1994).

observed to date. It is ∼4 orders of magnitude lower than the pure gas phase chemical model predictions of $X(O_2) \sim 7\times10^{-5}$.

Another option is to compare the O_2 column density directly with that of $C^{18}O$. These lines trace the part of the envelope where CO and, by inference, O_2 are not frozen out because of their similar binding energies (Collings et al. 2004; Acharyya et al. 2007). Using the $C^{18}O$ lines therefore provides an alternative constraint on the models. The $C^{18}O$ lines are also thermalized, and assuming a temperature of 30 K, its inferred column density is calculated as $(3.2–6.1)\times10^{14}$ cm^{-2}, depending on the adopted lines. The corresponding abundance ratio is $N(O_2)/N(C^{18}O) = \leq3.5$ so $N(O_2)/N(CO) \leq 6.4\times10^{-3}$ assuming CO/$C^{18}O$ = 550.

The critical densities for the NO transitions range from $n_{\rm cr\,NO(1)} = 2.4\times10^4$ cm^{-3} to $n_{\rm cr\,NO(4)} = 7.0\times10^3$ cm^{-3}), so LTE is again justified. For the 3σ upper limit on the NO (3) line in the 7.0 km s^{-1} component, the inferred column density is $N(NO) = <1.9\times10^{14}$ cm^{-2}, assuming $T_{\rm kin}$ = 30 K and no beam dilution. Thus, the implied NO abundance is $N(NO)/N(H_2) = X(NO) \leq 9.0\times10^{-10}$. All column densities and abundances associated with the protostellar source at $V_{\rm LSR}$ = 7.0 km s^{-1} are summarized in Table 3.

3.4.2. Abundance variation models

The above analysis assumes constant physical conditions along the line of sight as well as constant abundances. It is well known from multi-line observations of $C^{18}O$ that the CO abundance varies throughout the envelope, dropping by more than an order of magnitude in the cold freeze-out zone (e.g., Jørgensen et al. 2002; Yıldız et al. 2010, 2012). A more sophisticated analysis of the O_2 abundance is therefore obtained by using a model of the IRAS 4A envelope in which the density and temperature vary with position. The envelope structure presented in Fig. 6 has been determined by modeling the continuum emission (both the spectral energy distribution and the submillimeter spatial extent) using the 1D spherically symmetric dust radiative transfer code DUSTY (Ivezić & Elitzur 1997). A power-law density profile is assumed with an index p, i.e., $n \propto r^{-p}$, and the fitting method is described in Schöier et al. (2002) and Jørgensen et al. (2002, 2005), and is further discussed in Kristensen et al. (2012) with the caveats explained. The temperature is calculated as a function of position by solving for the dust radiative transfer through the assumed spherical envelopes, heated internally by the luminosity of the source. The gas temperature is assumed to be equal to the dust temperature. The envelope is defined from the inner radius of 33.5 AU up to the outer radius of 33 000 AU, where the density of the outer radius is 1×10^4 cm^{-3}. IRAS 4A is taken to be a standalone source; the possible overlap with IRAS 4B is ignored, but any material at large radii along the line of sight within the beam contributes in both the simulated and observed spectra.

The observed line intensities are used to constrain the molecular abundances in the envelope by assuming a trial abundance structure and computing the non-LTE excitation and line intensities with radiative transfer models for the given envelope structure. For this purpose, the Monte Carlo line radiative transfer program Ratran (Hogerheijde & van der Tak 2000) is employed. The simplest approach assumes a constant O_2 abundance through the envelope. Figure 7 (*left*) shows different abundance profiles, whereas Fig. 8 (*top left*) shows the resulting line intensities overplotted on the observed O_2 line. The light blue line in Figs. 7 and 8 is the maximum constant O_2 abundance that can be hidden in the noise, which is 2.5×10^{-8}. This is within a factor of 4 of the simple column density ratio estimate.

A more realistic abundance structure includes a freeze-out zone below 25 K where both O_2 and CO are removed from the gas. Such a CO "drop" abundance profile has been determined for the IRAS 4A envelope via the optically thin $C^{18}O$ lines from 1–0 to 10–9 in Yıldız et al. (2012). By using the best fit CO abundance structure and assuming a constant O_2/CO abundance ratio, an upper limit of $O_2/C^{18}O \leq 1$ is obtained (see red line in Figs. 7 and 8), corresponding to $O_2/CO \leq 2\times10^{-3}$.

With a 44″ beam, the 487 GHz line observed with HIFI is mostly sensitive to the bulk of the envelope. Nevertheless, the drop abundance models can be used to estimate the maximum O_2 abundance on smaller scales, to get a firm observational constraint on how much O_2 is in the region where it could enter the embedded circumstellar disk. The radius of such a disk is highly uncertain, but probably on the order of 100 AU (e.g. Visser et al. 2009). According to the drop abundance models, the maximum O_2 abundance that can be "hidden" inside 100 AU is $\sim10^{-6}$. However, the full chemical models from Sect. 4 suggest the actual O_2 abundance on these small scales is several orders of magnitude lower (Fig. 7, middle).

In summary, both the simple column density estimate and the more sophisticated envelope models imply a maximum O_2 abundance of $\sim10^{-8}$, and an O_2/CO ratio of $\leq2\times10^{-3}$. For NO, the best fit drop abundance requires NO to be about 8 times lower in abundance than $C^{18}O$, to be consistent with our NO non-detection.

4. Gas-grain models for the protostellar envelope

The next step in the analysis is to compare the upper limit for the $V_{\rm LSR}$ = 7.0 km s^{-1} component with full gas-grain chemical models. The Ohio State University (OSU) gas-grain network (Garrod et al. 2008) is used as the basis for the chemical network, which contains an extensive gas-grain chemistry. There are 590 gas phase and 247 grain surface species and 7500 reactions among

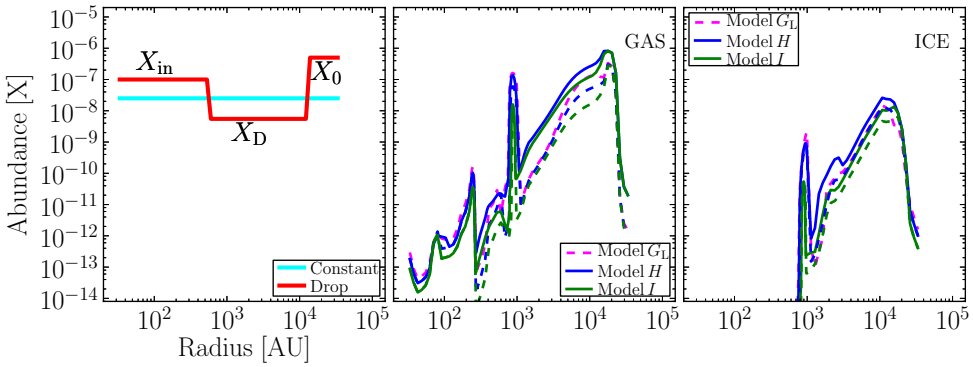

Fig. 7. *Left*: schematic diagram showing the best-fit drop abundance profile for O_2 (red line) assuming O_2 follows the same freeze-out and sublimation processes as $C^{18}O$. A constant (light blue) abundance profile is also shown. *Middle*: best-fit gaseous O_2 profiles obtained via gas-grain modeling. Models H_O and I_O are shown in solid lines and models H_L, I_L and G_L using a lower O + OH rate coefficient in dashed lines. As shown in Fig. 8 these are the maximum abundances of gaseous O_2 that can be hidden in the spectrum. *Right*: O_2 ice abundances for the best fit models. Solid lines show H_O and I_O whereas dashed lines are Models G_L, H_L and I_L.

Table 4. Rate coefficients for O_2 (Eq. (1)) and NO (Eq. (2)) formation.

No.	Species	T [K]	Rate coeff. [cm^3 s^{-1}]	References
1.[a]	O_2	39–149	3.5×10^{-11}	Carty et al. (2006)
2.[b]	O_2	10	7.8×10^{-12}	Lin et al. (2008)
3.[c]	O_2	10	5.4×10^{-13}	Xu et al. (2007)
4.	O_2	...	$7.5\times10^{-11}\times(T/300)^{-0.25}$	OSU database
5.	NO	...	$7.5\times10^{-11}\times(T/300)^{-0.18}$	OSU database

Notes. [(a)] CRESU measurement; [(b)] without J-shifting; [(c)] with J-shifting.

them. The subsequent subsections discuss the various chemical processes chemical processes that were considered in the network and are relevant for O_2 and NO are discussed.

4.1. Gas phase O_2 and NO formation

In the gas, O_2 is predominantly formed via reaction (1) between O atoms and OH radicals. The rate coefficient of this reaction has been measured in the temperature range between 39 K and 142 K with the CRESU (Cinetique de Reaction en Ecoulement Supersonique Uniforme) technique by Carty et al. (2006) who found a rate coefficient of 3.5×10^{-11} cm^3 s^{-1} that is constant with temperature. However, several theoretical calculations, especially below 39 K, also exist in the literature. Using quantum mechanical calculations with the so-called J-shifting approximation and neglecting non-adiabatic coupling, Xu et al. (2007) obtained a rate coefficient that decreases as the temperature drops from 100 to 10 K. At 10 K, the computed rate coefficient has fallen to a value of 5.4×10^{-13} cm^3 s^{-1}, significantly lower than the 39 K experimental value. However, more recent calculations by Lin et al. (2008), in which the J-shifting approximation has been removed, find a rate coefficient at 10 K of 7.8×10^{-12} cm^3 s^{-1}, higher than the Xu et al. (2007) value but still only about 1/4.5 of the experimental value at 39 K. The O_2 formation rates are summarised in Table 4. We have used all three rate coefficients to compare the computed O_2 abundance with the measured upper limit.

Gas-phase NO is predominantly formed through reaction (2). Its gas-phase reaction rate coefficient is listed in Table 4. This reaction is taken from the OSU database and was first determined by Smith et al. (2004).

4.2. Grain chemistry specific to O_2 and NO

The grain surface chemistry formulation in the OSU code follows the general description by Hasegawa & Herbst (1993) for

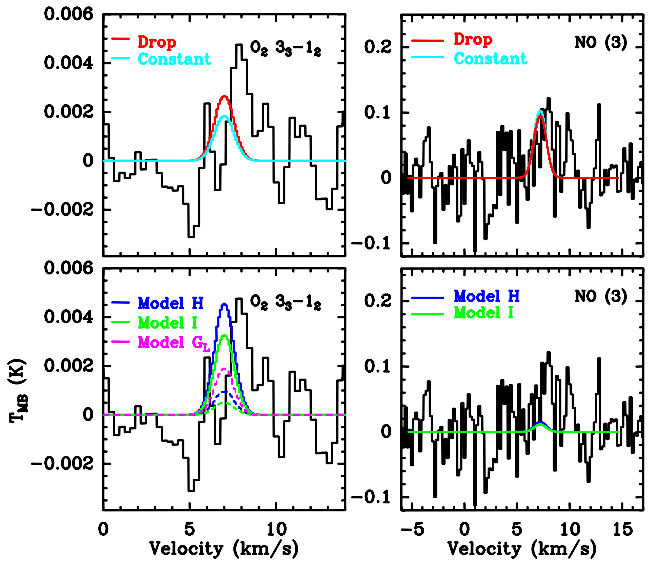

Fig. 8. Best-fit model spectra produced by different abundance profiles for O_2 3_3–1_2 and NO (3) are overplotted over the observed spectra. In the *buttom* figures, solid fit spectra show H_O and I_O models and dashed fit spectra show models H_L, I_L, and G_L. For NO, Case 2 is adopted.

adsorption, diffusion, reaction, dissociation, and desorption processes, updated and extended by Garrod et al. (2008). The binding energies of various species to the surface are critical parameters in the model. In most of the models, we adopt the binding energies from Garrod & Herbst (2006) appropriate for a water-rich ice surface. However, the possibility of a CO-rich ice surface is also investigated by reducing the binding energies by factors of 0.75 and 0.5, respectively (Bergin et al. 1995; Bergin & Langer 1997).

The presence of O_2 on an interstellar grain can be attributed to two different processes. First, gas-phase O_2 can be accreted on the grain surface during the (pre-)collapse phase and second, atomic oxygen can recombine to form O_2 on the dust grain via the following reaction:

$$O + O \rightarrow O_2. \quad (3)$$

Following Tielens & Hagen (1982), 800 K is used as the binding (desorption) energy for atomic oxygen on water ice. The binding energy for O_2 on water ice is taken as 1000 K (Cuppen & Herbst 2007), which is an average value obtained from the temperature programmed desorption (TPD) data by Ayotte et al. (2001) and Collings et al. (2004). A ratio of 0.5 between the diffusion barrier

and desorption energy has been assumed for the entire calculation (Cuppen & Herbst 2007), so the hopping energy for atomic oxygen is 400 K.

For this hopping energy, one oxygen atom requires 2×10^5 s to hop to another site at 10 K. For comparison, the time needed for a hydrogen atom to hop to another site is around 0.35 s, which is a factor of 10^6 faster. Therefore, instead of forming O_2, an accreted atomic oxygen species will be hydrogenated, leading to the formation of OH and H_2O. It is most unlikely that accreted atomic oxygen produces any significant amount of O_2 on the grain surface during the pre-collapse phase. Recent studies using the continuous time random walk (CTRW) Monte Carlo method do not produce significant O_2 on the grain surface (Cuppen & Herbst 2007). However, elevated grain temperatures ($\gtrsim$20 K), when the residence time of an H atom on the grain is very short and atomic oxygen has enhanced mobility, could be conducive to O_2 formation.

What happens to the O_2 that is formed in the gas phase and accreted onto the dust grains? There are two major destruction pathways. First, the reaction of O_2 with atomic H leads to the formation of HO_2 and H_2O_2, which then could be converted to water following reaction pathways suggested by Ioppolo et al. (2008) and Cuppen et al. (2010):

$$O_2 \xrightarrow{H} HO_2 \xrightarrow{H} H_2O_2 \xrightarrow{H} H_2O + OH. \quad (4)$$

Thus, a longer cold pre-collapse phase would significantly reduce O_2 on the dust grains and turn it into water ice, whereas a shorter pre-collapse phase would yield a higher solid O_2 abundance (Roberts & Herbst 2002). These reactions also depend on the grain temperature: at higher temperatures, the shorter residence time of H atoms on the grain leads to less conversion of O_2.

The second destruction route leads to the formation of ozone through

$$O_2 + O \rightarrow O_3. \quad (5)$$

This route is most effective at slightly higher grain temperatures ($\gtrsim$20 K) when atomic oxygen has sufficient mobility to find an O_2 molecule before it gets hydrogenated. Ozone could also be hydrogenated as suggested by Tielens & Hagen (1982) and confirmed in the laboratory by Mokrane et al. (2009) and Romanzin et al. (2010) leading back to O_2:

$$O_3 \xrightarrow{H} O_2 + OH. \quad (6)$$

Similarly, accreted NO on the grain surface can undergo various reactions. In particular, recent laboratory experiments have shown that NO is rapidly hydrogenated to NH_2OH at low ice temperatures (Congiu et al. 2012). A critical parameter here is the competition of the different channels for reaction of HNO + H, which can either go back to NO + H_2 or form H_2NO.

The final important ingredient of the gas-grain chemistry is the rate at which molecules are returned from the ice back into the gas phase. Both thermal and non-thermal desorption processes are considered. The first non-thermal process is reactive desorption; here the exothermicity of the reaction is channeled into the desorption of the product with an efficiency determined by a parameter $a_{\rm RRK}$ (Garrod et al. 2007). In these model runs, a value of 0.01 is used, which roughly translates into an efficiency of 1%. Recently, Du et al. (2012) used 7% for the formation of H_2O_2.

Second, there is desorption initiated by UV absorption. Photodissociation of an ice molecule produces two atomic or radical products, which can subsequently recombine and desorb via the reactive desorption mechanism. The photons for this process derive both from the external radiation field and from UV photons generated by ionization of H_2 due to cosmic rays, followed by the excitation of H_2 by secondary electrons. The externally generated UV photons are very effective in diffuse and translucent clouds but their role in dense clouds is limited to the edge of the core (Ruffle & Herbst 2000; Hollenbach et al. 2009). The cosmic-ray-generated internal photons can play an effective role in the dense envelope, with a photon flux of $\approx 10^4$ photons cm^{-2} s^{-1} (Shen et al. 2004). We have considered both sources of radiation in our model. In either case, the rate coefficients for photodissociation on surfaces are assumed to be the same as in the gas phase.

Photodesorption can proceed both by the recombination mechanism described above as well as by kick-out of a neighboring molecule. The combined yields for a variety of species including CO and H_2O have been measured in the laboratory (Öberg et al. 2009a,b; Muñoz Caro et al. 2010) and computed through molecular dynamics simulations for the case of H_2O by Andersson & van Dishoeck (2008) and Arasa et al. (2010). Finally, there is the heating of grains via direct cosmic ray bombardment, which is effective for weakly bound species like CO and O_2 and included following the formulae and parameters of Hasegawa & Herbst (1993).

4.3. Model results

Our physical models have two stages, the "pre-collapse stage" and the "protostellar stage". In the pre-collapse stage, the hydrogen density is $n_{\rm H} = 10^5$ cm^{-3}, visual extinction $A_{\rm V} = 10$ mag, the cosmic-ray ionization parameter, $\zeta = 1.3 \times 10^{17}$ s^{-1}, and the (gas and grain) temperature, $T = 10$ K, which are standard parameters representative of cold cores. The initial elemental abundances of carbon, oxygen and nitrogen are 7.30×10^{-5}, 1.76×10^{-4} and 2.14×10^{-5}, respectively, in the form of atomic C^+, O and N. All hydrogen is assumed to be in molecular form initially. In the second stage, the output abundance of the first phase is used as the initial abundance at each radial distance with the density, temperature and visual extinction parameters at each radius taken from the IRAS 4A model shown in Fig. 6. We assume that the transition to the protostellar phase from the pre-collapse stage is instantaneous i.e., the power-law density and temperature structure are established quickly, consistent with evolutionary models (Lee et al. 2004; Young & Evans 2005).

To explain the observed spectra of O_2, both the pre-collapse time and protostellar time as well as the O_2 formation rates are varied. Analysis of CO and HCO^+ multi-line observations in pre- and protostellar sources have shown that the high density pre-collapse stage typically lasts a few $\times 10^5$ yr (e.g., Jørgensen et al. 2005; Ward-Thompson et al. 2007). The models *A* to *Q* have different parameters and timescales which are listed in Table 5. Those models result in abundance profiles in the envelope at each time step and radius. These profiles are then run in `Ratran` in order to compare directly with the observations.

Figure 7 (*middle*) shows examples of model abundance profiles. All model runs predict lower O_2 abundances than the evolutionary models of Visser et al. (2011), whose chemical network did not include any grain-surface processing of O_2. The line emission from our models is compared to the observations in Fig. 8 (bottom left). Table 5 summarizes the resulting O_2 peak temperatures for each of the models. All models except *H* and *I* overproduce the observed O_2 emission of at most a few mK, by up to two orders of magnitude in the peak temperature.

Table 5. Chemical models considered for the IRAS 4A protostellar envelope

Model	Pre-collapse stage [yr]	Protostellar stage [yr]	O_2 formation rate [cm^3 s^{-1}]	$T_{peak}(O_2)^a$ [K]	$T_{peak}(NO)^a$ [K]
A	5×10^4	10^5	$7.5\times10^{-11}\times(T/300)^{-0.25}$	0.119	...
B	1×10^5	10^5	$7.5\times10^{-11}\times(T/300)^{-0.25}$	0.102	...
C	2×10^5	10^5	$7.5\times10^{-11}\times(T/300)^{-0.25}$	0.085	...
D	3×10^5	10^5	$7.5\times10^{-11}\times(T/300)^{-0.25}$	0.073	...
E	5×10^5	10^5	$7.5\times10^{-11}\times(T/300)^{-0.25}$	0.042	...
F	6×10^5	10^5	$7.5\times10^{-11}\times(T/300)^{-0.25}$	0.024	...
G_O	7×10^5	10^5	$7.5\times10^{-11}\times(T/300)^{-0.25}$	0.011	...
$G_L{}^b$	7×10^5	10^5	7.84×10^{-12}	0.0019	...
$H_O{}^b$	8×10^5	10^5	$7.5\times10^{-11}\times(T/300)^{-0.25}$	0.0046	0.015
$H_C{}^b$	8×10^5	10^5	3.50×10^{-11}	0.0025	...
$H_L{}^b$	8×10^5	10^5	7.84×10^{-12}	0.0010	...
$I_O{}^b$	1×10^6	10^5	$7.5\times10^{-11}\times(T/300)^{-0.25}$	0.0033	0.011
$I_C{}^b$	1×10^6	10^5	3.50×10^{-11}	0.0014	...
$I_L{}^b$	1×10^6	10^5	7.84×10^{-12}	0.0005	...
J	8×10^4	2×10^4	3.50×10^{-11}	0.106	...
L	3×10^5	10^5	3.50×10^{-11}	0.063	...
M	3×10^5	10^5	7.84×10^{-12}	0.047	...
N	3×10^5	10^5	5.40×10^{-13}	0.018	...
O	5×10^5	10^5	3.50×10^{-11}	0.031	...
P	5×10^5	10^5	7.84×10^{-12}	0.020	...
Q	5×10^5	10^5	5.40×10^{-13}	0.0068	0.091

Notes. Models *G*, *H*, and *I* use different rate coefficients for O_2 formation (Eq. (1)), as indicated by subscripts: O for OSU, C for Carty et al. (2006), and L for Lin et al. (2008). [(a)] Ratran model results using a line width of 1.0 km s^{-1}. [(b)] Best fit models. For NO, Case 2 is tabulated.

The models that are consistent with the data have in common longer pre-collapse stages; in particular Model *I*, which has the longest pre-collapse stage of 10^6 years, best fits the 3σ O_2 limit. Using a lower rate coefficient for the O+OH reaction of 7.84×10^{-12} cm^3 s^{-1} (Lin et al. 2008) for the same best fit models (H_L and I_L) results in a factor of 5 lower emission. In this case, the pre-collapse stage can be shortened to $\sim7\times10^5$ yr (Model G_L).

For NO, the *H* and *I* models were calculated twice. In Case 1, hydrogenation of HNO leads back to NO and H_2 and in Case 2 hydrogenation of HNO leads to H_2NO as suggested by Congiu et al. (2012). Comparison of the results from Case 1 with observations shows significant overproduction of the observed NO emission, whereas Case 2 is consistent with an upper limit of 0.05 K (1σ). Therefore, a combination of both reactions appears to be needed.

These results for IRAS 4A suggest that a long pre-collapse stage is characteristic of the earliest stages of star formation, in which atomic and molecular oxygen are frozen-out onto the dust grains and converted into water ice, as proposed by Bergin et al. (2000). Similarly, the rapid conversion of NO to other species on the grains limits its gas-phase abundance. It is clear that the grain surface processes are much more important than those of the pure gas-phase chemistry in explaining the O_2 and NO observations. The timescale for NGC 1333 IRAS 4A is at the long end of that inferred more generally from observations.

The model results show that the fraction of O_2 in the gas and left on the grains must indeed be very small, dropping to $\leq10^{-9}$ close to the protostar (Fig. 7, right). This in turn implies that the gas and ice that enter the disk are very poor in O_2. Although IRAS 4A is the only low-mass protostar that has been observed to this depth, the conclusions drawn for IRAS 4A probably hold more generally. Thus, unless there is significant production of O_2 in the disk, the icy planetesimals will also be poor in O_2.

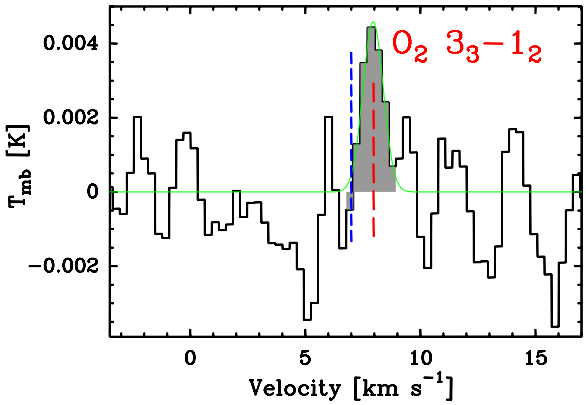

Fig. 9. Tentative detection of the O_2 3_3–1_2 line from the extended NGC 1333 cloud. The blue line indicates the source velocity of IRAS 4A at 7.0 km s^{-1} and the red line indicates the extended cloud V_{LSR} at 8.0 km s^{-1}. The green line indicates a Gaussian fit to the component at 8.0 km s^{-1}.

5. Tentative detection of O_2 in the 8 km s^{-1} cloud

Although there is no sign of O_2 emission at the velocity of the dense protostellar envelope (7.0 km s^{-1}), a 4.5σ tentative detection of O_2 3_3–1_2 line emission is found at $V_{LSR}=8.0$ km s^{-1}, the velocity of the more extended NGC 1333 molecular cloud (Fig. 9; Loren 1976; Liseau et al. 1988). The feature is also seen in individual *H* and *V* polarization spectra. The peak intensity of the tentative detection is $T_{mb}=4.6$ mK, the line width $\Delta V=1.3$ km s^{-1}, and the integrated intensity is $\int T_{mb}dV=6.9$ mK km s^{-1} between the velocities of 6.5 to 9.7 km s^{-1}. The large HIFI beam size of 44″ encompasses both the extended cloud as well as the compact envelope. Since any O_2 emission is optically thin, the two components cannot block each other, even if slightly overlapping in velocity.

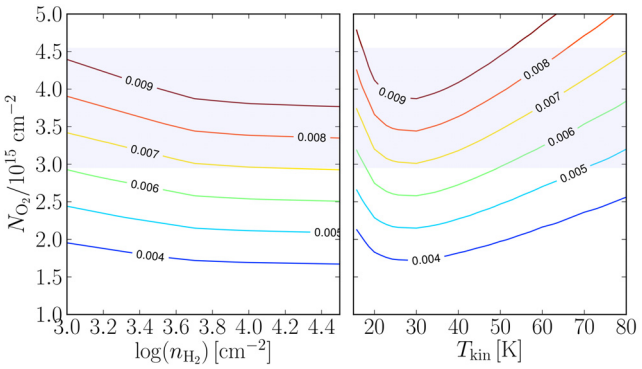

Fig. 10. Integrated intensities of O_2 are shown as contours for a range of model column densities as function of density (*left*) and temperature (*right*) for the 8.0 km s^{-1} component. The yellow solid line is the observed integrated intensity of the tentative detection and the shaded region represents the range of column densities for their corresponding temperatures. *Left*: T_{kin} = 30 K is assumed for different densities and *right*: $n = 5 \times 10^3$ cm^{-3} is assumed for different temperatures.

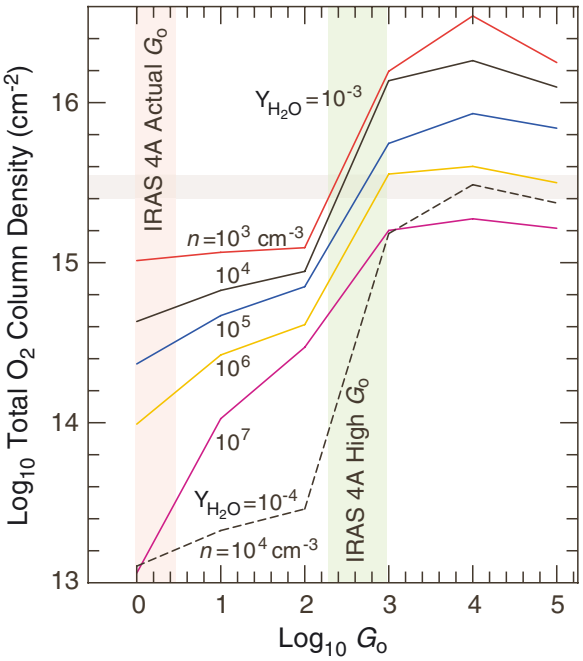

Fig. 11. Total O_2 column density as a function of G_o and density (adapted from Melnick et al. 2012; Hollenbach et al. 2009) for the 8.0 km s^{-1} component. The horizontal grey band shows the total O_2 column density range for the observed integrated intensity in the 8 km s^{-1} component. The vertical green band presents the range of high-G_0 values required to produce this range of O_2 column densities for gas densities between 10^3 cm^{-3} and 10^7 cm^{-3}, whereas the orange band presents the actual G_0. Y_{H_2O} is the water ice photodesorption yield.

The density in the surrounding cloud at 8.0 km s^{-1} is expected to be significantly lower than that in the envelope. Figure B.1 presents the C^{18}O 3–2/1–0 ratio for the 8.0 km s^{-1} component. The observed value is consistent with a wide range of kinetic temperatures from 20 K to 70 K, with corresponding densities in a narrow range from 7×10^3 to 2×10^3 cm^{-3}, respectively. C^{18}O column densities from the 3–2 and 1–0 line intensities are then $(2.3–1.8) \times 10^{15}$ cm^{-2} for this range of physical parameters.

For the same range of conditions, the O_2 column density is $(2.8–4.3) \times 10^{15}$ cm^{-2} (Fig. 10). The inferred abundance ratios are $N(O_2)/N(C^{18}O) = 1.2$ to 2.4, and $N(O_2)/N(CO) = (2.2–4.3) \times 10^{-3}$. Assuming CO/H$_2 \approx 10^{-4}$ gives $N(O_2)/N(H_2) = (2.2–4.3) \times 10^{-7}$. Interestingly, the inferred O_2 abundance is in between the values found for the Orion and ρ Oph A clouds (Goldsmith et al. 2011; Liseau et al. 2012). By assuming T_{kin} = 30 K, the implied NO column density is 2.3×10^{14} cm^{-2}, leading to $N(NO)/N(O_2) = (5.3–8.1) \times 10^{-2}$ and $N(NO)/N(H_2) = 2.3 \times 10^{-8}$.

Can such an O_2 column density and abundance be reproduced by chemical models? For the surrounding cloud, a large gas-grain model is not needed. Instead, the PDR models of Hollenbach et al. (2009), which include a simplified gas-grain chemistry, are adequate to model the emission. Figure 11 is a plot adapted from Melnick et al. (2012), which shows the values of interstellar radiation field G_0 required to reproduce the range of O_2 column densities according to the model described in Hollenbach et al. (2009). The horizontal grey band bounds the total observed O_2 column density range of $(2.8–4.3) \times 10^{15}$ cm^{-2}, while the vertical green band shows the range of G_0 values required to produce this range of O_2 column densities for gas densities between 10^3 cm^{-3} and 10^7 cm^{-3}. For our low inferred densities of $<10^4$ cm^{-3}, a high G_0 value of 300–650 fits the data. There is no external source in the NGC 1333 region which can provide this level of UV illumination, not even the nearby B8 V type star BD+30°549 (α = 3^{h}29^{m}19^s.78, δ = +31°24′57″.05 (J2000); ~0.8 pc away; van Leeuwen 2007). The G_0 value from this star at our position is at most 2.8 and can therefore not explain the high-G_0 scenario. Models with a slightly higher (factor of 2) water ice photodesorption yield than the standard value of $Y_{H_2O} = 10^{-3}$ would fit better the low-G_0 regime, where the value of G_0 is between the interstellar value of 1 and 2.8. This value of Y_{H_2O} is within the uncertainties of the laboratory (Öberg et al. 2009a) and theoretical work (Arasa et al. 2010). More generally, a factor of two uncertainty in abundance can readily result from the combined uncertainties of the individual rate coefficients that lead to O_2 formation and destruction (Wakelam et al. 2006), so it does not necessarily imply an increased value of Y_{H_2O}. Considering the uncertainties in rate coefficients as well as possible increase in Y, there does not seem to be a problem having the actual low value of G_0 produce the observed column density of molecular oxygen.

6. Conclusions

We have presented the first deep (7.7 h) *Herschel*-HIFI observations of the O_2 3_3–1_2 line at 487 GHz towards a deeply embedded Class 0 protostar, NGC 1333 IRAS 4A. The results from the observations and models can be summarized as follows.

- No O_2 emission is detected from the protostellar envelope, down to a 3σ upper limit of $X(O_2) \lesssim 6 \times 10^{-9}$, the lowest O_2 abundance limit toward a protostar to date. The O_2/CO limit is $\leq 6 \times 10^{-3}$.
- A full gas-grain chemical model coupled with the physical structure of the envelope is compared to our data consisting of two stages, a "pre-collapse stage" and "protostellar stage". Best fits to the observed upper limit on the O_2 line suggest a long pre-collapse stage (~0.7–1 $\times 10^6$ years), during which atomic oxygen is frozen out onto the dust grains and converted into water ice. Also, at least a fraction of NO must be converted to more complex nitrogen species in the ice.
- The low O_2 abundance in the gas and on the grains in the inner envelope implies that the material entering the disk is very poor in O_2.

- A 4.5σ tentative O_2 detection is found at $V_{LSR} = 8.0$ km s^{-1}, which is interpreted as emission originating from the surrounding more extended NGC 1333 cloud. At this velocity, also a weak NO line is seen.
- Comparison with PDR models of Hollenbach et al. (2009) suggests a high G_0 of 300–650 in the surrounding cloud for the low inferred density of $<10^4$ cm^{-3}. For the low G_0 inferred at our position, either the H_2O ice photodesorption yield would need to be increased by a factor of ∼2 or combination of other minor changes in reaction rates would be needed to reproduce the observed $N(O_2)$ with a reasonable value of G_0.

Acknowledgements. U.A.Y. and astrochemistry in Leiden are supported by the Netherlands Research School for Astronomy (NOVA), by a Spinoza grant and grant 614.001.008 from the Netherlands Organisation for Scientific Research (NWO), and by the European Community's Seventh Framework Programme FP7/2007–2013 under grant agreement 238258 (LASSIE) and 291141 (CHEMPLAN). This work was carried out in part at the Jet Propulsion Laboratory, which is operated by the California Institute of Technology under contract with NASA. The authors are grateful to many funding agencies and the HIFI-ICC staff, who has been contributing for the construction of *Herschel* and HIFI for many years. HIFI has been designed and built by a consortium of institutes and university departments from across Europe, Canada and the United States under the leadership of SRON Netherlands Institute for Space Research, Groningen, The Netherlands and with major contributions from Germany, France and the US. Consortium members are: Canada: CSA, U.Waterloo; France: CESR, LAB, LERMA, IRAM; Germany: KOSMA, MPIfR, MPS; Ireland, NUI Maynooth; Italy: ASI, IFSI-INAF, Osservatorio Astrofisico di Arcetri- INAF; Netherlands: SRON, TUD; Poland: CAMK, CBK; Spain: Observatorio Astronómico Nacional (IGN), Centro de Astrobiología (CSIC-INTA). Sweden: Chalmers University of Technology – MC2, RSS & GARD; Onsala Space Observatory; Swedish National Space Board, Stockholm University – Stockholm Observatory; Switzerland: ETH Zurich, FHNW; USA: Caltech, NASA/JPL, NHSC.

References

Acharyya, K., Fuchs, G. W., Fraser, H. J., van Dishoeck, E. F., & Linnartz, H. 2007, A&A, 466, 1005
Andersson, S., & van Dishoeck, E. F. 2008, A&A, 491, 907
André, P., & Montmerle, T. 1994, ApJ, 420, 837
Arasa, C., Andersson, S., Cuppen, H. M., van Dishoeck, E. F., & Kroes, G.-J. 2010, J. Chem. Phys., 132, 184510
Ayotte, P., Scott, S. R., Stevenson, K. P., et al. 2001, J. Geophys. Res., 106, 33387
Bergin, E. A., & Langer, W. D. 1997, ApJ, 486, 316
Bergin, E. A., Langer, W. D., & Goldsmith, P. F. 1995, ApJ, 441, 222
Bergin, E. A., Melnick, G. J., Stauffer, J. R., et al. 2000, ApJ, 539, L129
Black, J. H., & Smith, P. L. 1984, ApJ, 277, 562
Blake, G. A., Sandell, G., van Dishoeck, E. F., et al. 1995, ApJ, 441, 689
Bottinelli, S., Ceccarelli, C., Williams, J. P., & Lefloch, B. 2007, A&A, 463, 601
Carty, D., Goddard, A., Kohler, S., Sims, I., & Smith, I. 2006, J. Phys. Chem. A, 110, 3101
Collings, M. P., Anderson, M. A., Chen, R., et al. 2004, MNRAS, 354, 1133
Congiu, E., Fedoseev, G., Ioppolo, S., et al. 2012, ApJ, 750, L12
Cuppen, H. M., & Herbst, E. 2007, ApJ, 668, 294
Cuppen, H. M., Ioppolo, S., Romanzin, C., & Linnartz, H. 2010, Phys. Chem. Chem. Phys., 12, 12077
Curtis, E. I., Richer, J. S., & Buckle, J. V. 2010, MNRAS, 401, 455
de Graauw, T., Helmich, F. P., Phillips, T. G., et al. 2010, A&A, 518, L6
Doty, S. D., Schöier, F. L., & van Dishoeck, E. F. 2004, A&A, 418, 1021
Drouin, B. J., Yu, S., Miller, C. E., et al. 2010, J. Quant. Spectrosc. Rad. Trans., 111, 1167
Du, F., Parise, B., & Bergman, P. 2012, A&A, 538, A91
Garrod, R. T., & Herbst, E. 2006, A&A, 457, 927
Garrod, R. T., Wakelam, V., & Herbst, E. 2007, A&A, 467, 1103
Garrod, R. T., Weaver, S. L. W., & Herbst, E. 2008, ApJ, 682, 283
Goldsmith, P. F., Snell, R. L., Erickson, N. R., et al. 1985, ApJ, 289, 613
Goldsmith, P. F., Melnick, G. J., Bergin, E. A., et al. 2000, ApJ, 539, L123
Goldsmith, P. F., Liseau, R., Bell, T. A., et al. 2011, ApJ, 737, 96
Gutermuth, R. A., Myers, P. C., Megeath, S. T., et al. 2008, ApJ, 674, 336
Hasegawa, T. I., & Herbst, E. 1993, MNRAS, 261, 83
Herbst, E., & Klemperer, W. 1973, ApJ, 185, 505
Hirota, T., Bushimata, T., Choi, Y. K., et al. 2008, PASJ, 60, 37
Hogerheijde, M. R., & van der Tak, F. F. S. 2000, A&A, 362, 697
Hollenbach, D., Kaufman, M. J., Bergin, E. A., & Melnick, G. J. 2009, ApJ, 690, 1497
Ioppolo, S., Cuppen, H. M., Romanzin, C., van Dishoeck, E. F., & Linnartz, H. 2008, ApJ, 686, 1474
Ivezić, Z., & Elitzur, M. 1997, MNRAS, 287, 799
Jørgensen, J. K., Schöier, F. L., & van Dishoeck, E. F. 2002, A&A, 389, 908
Jørgensen, J. K., Schöier, F. L., & van Dishoeck, E. F. 2005, A&A, 437, 501
Jørgensen, J. K., van Dishoeck, E. F., Visser, R., et al. 2009, A&A, 507, 861
Kristensen, L. E., Visser, R., van Dishoeck, E. F., et al. 2010, A&A, 521, L30
Kristensen, L. E., van Dishoeck, E. F., Bergin, E. A., et al. 2012, A&A, 542, A8
Kutner, M. L., & Ulich, B. L. 1981, ApJ, 250, 341
Larsson, B., Liseau, R., Pagani, L., et al. 2007, A&A, 466, 999
Lee, J.-E., Bergin, E. A., & Evans, II, N. J. 2004, ApJ, 617, 360
Lefloch, B., Castets, A., Cernicharo, J., & Loinard, L. 1998, ApJ, 504, L109
Lin, S. Y., Guo, H., Honvault, P., Xu, C., & Xie, D. 2008, J. Chem. Phys., 128
Lique, F. 2010, J. Chem. Phys., 132, 044311
Liseau, R., Sandell, G., & Knee, L. B. G. 1988, A&A, 192, 153
Liseau, R., Goldsmith, P. F., Larsson, B., et al. 2012, A&A, 541, A73
Loren, R. B. 1976, ApJ, 209, 466
Maret, S., Ceccarelli, C., Tielens, A. G. G. M., et al. 2005, A&A, 442, 527
Melnick, G. J., Stauffer, J. R., Ashby, M. L. N., et al. 2000, ApJ, 539, L77
Melnick, G. J., Tolls, V., Goldsmith, P. F., et al. 2012, ApJ, 752, 26
Mokrane, H., Chaabouni, H., Accolla, M., et al. 2009, ApJ, 705, L195
Muñoz Caro, G. M., Jiménez-Escobar, A., Martín-Gago, J. Á., et al. 2010, A&A, 522, A108
Müller, H. S. P., Schlöder, F., Stutzki, J., & Winnewisser, G. 2005, J. Mol. Struct., 742, 215
Nordh, H. L., von Schéele, F., Frisk, U., et al. 2003, A&A, 402, L21
Öberg, K. I., Linnartz, H., Visser, R., & van Dishoeck, E. F. 2009a, ApJ, 693, 1209
Öberg, K. I., van Dishoeck, E. F., & Linnartz, H. 2009b, A&A, 496, 281
Ott, S. 2010, in Astronomical Data Analysis Software and Systems XIX, eds. Y. Mizumoto, K.-I. Morita, & M. Ohishi, ASP Conf. Ser., 434, 139
Pagani, L., Langer, W. D., & Castets, A. 1993, A&A, 274, L13
Pagani, L., Olofsson, A. O. H., Bergman, P., et al. 2003, A&A, 402, L77
Pickett, H. M., Poynter, R. L., Cohen, E. A., et al. 2010, J. Quant. Spectr. Rad. Trans., 111, 1617
Pilbratt, G. L., Riedinger, J. R., Passvogel, T., et al. 2010, A&A, 518, L1
Roberts, H., & Herbst, E. 2002, A&A, 395, 233
Roelfsema, P. R., Helmich, F. P., Teyssier, D., et al. 2012, A&A, 537, A17
Romanzin, C., Arzoumanian, E., Es-Sebbar, E., et al. 2010, Planet. Space Sci., 58, 1748
Ruffle, D. P., & Herbst, E. 2000, MNRAS, 319, 837
Schöier, F. L., Jørgensen, J. K., van Dishoeck, E. F., & Blake, G. A. 2002, A&A, 390, 1001
Schöier, F. L., van der Tak, F. F. S., van Dishoeck, E. F., & Black, J. H. 2005, A&A, 432, 369
Shen, C. J., Greenberg, J. M., Schutte, W. A., & van Dishoeck, E. F. 2004, A&A, 415, 203
Smith, I. W. M., Herbst, E., & Chang, Q. 2004, MNRAS, 350, 323
Tielens, A. G. G. M., & Hagen, W. 1982, A&A, 114, 245
Černis, K. 1990, Ap&SS, 166, 315
van der Tak, F. F. S., Black, J. H., Schöier, F. L., Jansen, D. J., & van Dishoeck, E. F. 2007, A&A, 468, 627
van Dishoeck, E. F., Kristensen, L. E., Benz, A. O., et al. 2011, PASP, 123, 138
van Leeuwen, F. 2007, A&A, 474, 653
Visser, R., van Dishoeck, E. F., Doty, S. D., & Dullemond, C. P. 2009, A&A, 495, 881
Visser, R., Doty, S. D., & van Dishoeck, E. F. 2011, A&A, 534, A132
Wakelam, V., Herbst, E., Selsis, F., & Massacrier, G. 2006, A&A, 459, 813
Ward-Thompson, D., André, P., Crutcher, R., et al. 2007, Protostars and Planets V, 33
Wilson, T. L., & Rood, R. 1994, ARA&A, 32, 191
Woodall, J., Agúndez, M., Markwick-Kemper, A. J., & Millar, T. J. 2007, A&A, 466, 1197
Xu, C., Xie, D., Honvault, P., Lin, S. Y., & Guo, H. 2007, J. Chem. Phys., 127
Yıldız, U. A., van Dishoeck, E. F., Kristensen, L. E., et al. 2010, A&A, 521, L40
Yıldız, U. A., Kristensen, L. E., van Dishoeck, E. F., et al. 2012, A&A, 542, A86
Young, C. H., & Evans, II, N. J. 2005, ApJ, 627, 293

Pages 12 to 13 are available in the electronic edition of the journal at http://www.aanda.org

Appendix A: HIFI O_2 spectrum

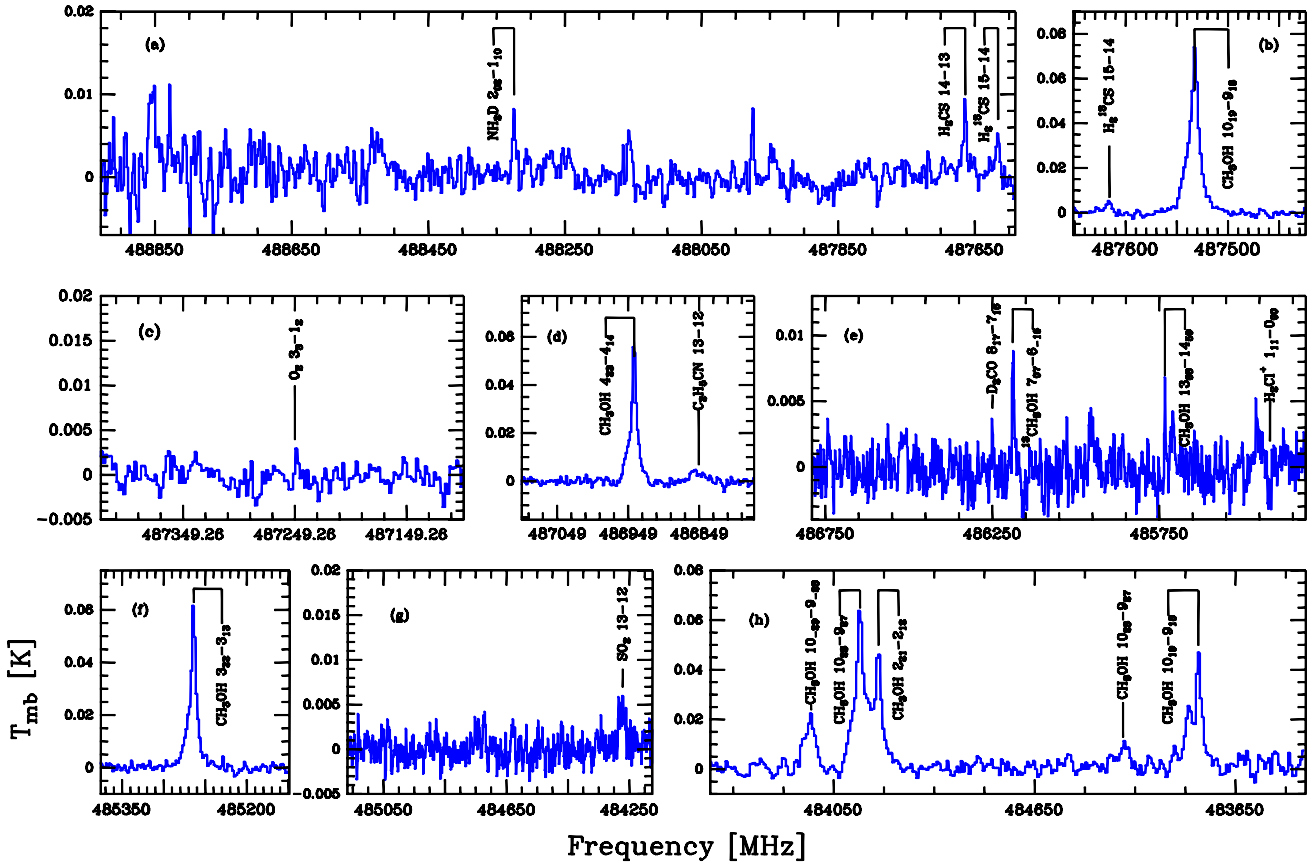

Fig. A.1. Spectrum of Fig. 2 magnified over certain velocity ranges. In panel **c)** the O_2 3_3–1_2 transition is shown. Identifications refer to the 7.0 km s^{-1} component.

Table A.1. Overview of the other lines observed in the same spectrum.

Mol.	Trans. J_u–J_l	E_u/k_B [K]	A_{ul} [s^{-1}]	Frequency [GHz]	$\int T_{MB}dV$ [mK km s^{-1}]	T_{peak} [mK]	*FWHM* [km s^{-1}]
NH_2D	2_{02}–1_{10}	47.2	1.36×10^{-4}	488.323810	25	10	3.4
H_2CS	14–13	188.8	1.76×10^{-3}	487.663321	28	9	3.3
$H_2^{13}CS$	15–14	200.5	1.77×10^{-3}	487.615288	22	5	3.9
CH_3OH	10_{19}–9_{18}	143.3	5.15×10^{-4}	487.531887	580	80	8.2
O_2	3_3–1_2	26.38	8.66×10^{-9}	487.249264	7	...	...
CH_3OH	4_{23}–4_{14}	60.9	5.45×10^{-4}	486.940837	390	60	7.2
C_2H_5CN	13–12	66.9	1.00×10^{-6}	486.849912	36	5	7.3
D_2CO	8_{17}–7_{16}	111.0	3.36×10^{-3}	486.248662	9	7	1.1
$^{13}CH_3OH$	7_{07}–6_{16}	76.5	3.02×10^{-4}	486.188242	39	10	3.9
CH_3OH	13_{68}–14_{59}	404.8	1.16×10^{-4}	485.732280	12	10	1.4
H_2Cl^+	1_{11}–0_{00}	...	...	485.420796	−5	−6	0.8
CH_3OH	3_{22}–3_{13}	51.6	5.02×10^{-4}	485.263263	401	71	7.3
SO_2	13–12	105.8	5.42×10^{-4}	484.270879	26	6	1.1
CH_3OH	10_{-29}–9_{-28}	153.6	4.88×10^{-4}	484.071775	170	20	8.4
CH_3OH	10_{28}–9_{27}	150.0	4.83×10^{-4}	484.023168	490	70	8.2
CH_3OH	2_{21}–2_{12}	44.7	3.99×10^{-4}	484.004740	280	50	4.9
CH_3OH	10_{28}–9_{27}	165.4	4.90×10^{-4}	483.761387	70	10	5.8
CH_3OH	10_{19}–9_{18}	148.7	5.13×10^{-4}	483.686308	210	50	4.2

Notes. The level energies, Einstein A coefficients, and line frequencies are from the LAMDA, JPL and CDMS databases (Schöier et al. 2005; Pickett et al. 2010; Müller et al. 2005). Rms is 1.3 mK and in 0.35 km s^{-1} bin. Identifications refer to the 7.0 km s^{-1} component.

Appendix B: RADEX calculations for $C^{18}O$

The integrated intensity ratio of $C^{18}O$ 3–2/1–0 is equal to 0.74 for the 8.0 km s^{-1} component. This ratio can be analysed using the RADEX non-LTE excitation and radiative transfer program (van der Tak et al. 2007) to constrain the physical parameters. Figure B.1 presents the integrated intensity ratios as function of temperature and density, obtained for optically thin conditions. The observed ratio is indicated in dash-dotted lines.

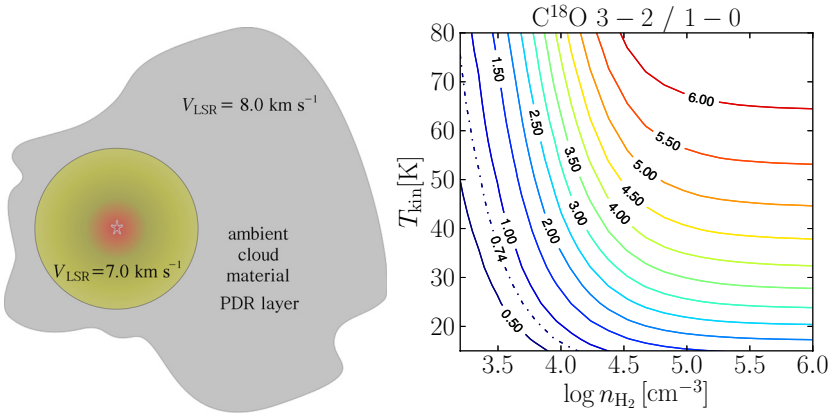

Fig. B.1. *Left*: schematic cartoon showing the scenario of O_2 emission originating from the surrounding cloud. *Right*: integrated intensity ratios calculated with RADEX, as function of temperature and density, for a $C^{18}O$ column density of 5×10^{14} cm^{-2} (optically thin conditions). The $C^{18}O$ 3–2/1–0 ratio is relevant for the surrounding NGC 1333 cloud, which is traced by the 8.0 km s^{-1} component. Dash-dotted lines indicate the observed ratio of $C^{18}O$ 3–2/1–0 = 0.74 for the V_{LSR} = 8.0 km s^{-1} component.